

Scanning-free compressive reconstruction of
object motion with sub-pixel accuracy

by

Yi Liu

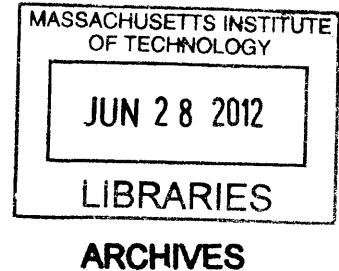
Submitted to the Department of Mechanical Engineering
in partial fulfillment of the requirements for the degree of

Master of Science in Mechanical Engineering

at the

MASSACHUSETTS INSTITUTE OF TECHNOLOGY

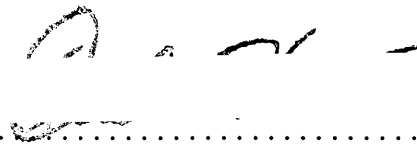
June 2012



© Massachusetts Institute of Technology 2012. All rights reserved.

Author
Department of Mechanical Engineering
May 10th, 2012

Certified by 
George Barbastathis
Professor
Thesis Supervisor


Accepted by
David E. Hardt
Chairman, Department Committee on Graduate Theses

**Scanning-free compressive reconstruction of object motion
with sub-pixel accuracy**

by

Yi Liu

Submitted to the Department of Mechanical Engineering
on May 10th, 2012, in partial fulfillment of the
requirements for the degree of
Master of Science in Mechanical Engineering

Abstract

Sub-pixel movement detection is an under-sampling problem. The basic idea for successful detection is to spread out the information over a larger sampling region. Diffraction provides a natural way to spread out the information; however, conventional digital holographic methods are not effective for extracting sub-pixel accuracy. Here we show how to apply compressive reconstruction to the same problem effectively.

Compressed sensing is a new framework to systematically find highly accurate solutions to an under-sampled linear system. To guarantee the accuracy of reconstruction result, compressed sensing requires that the unknown has to be sparse in some predetermined basis. In our study, for the one dimensional sub-pixel movement detection, we propose to use the derivative operator as the sparsifying basis. We implemented the derivative operator to the hologram and applied a sparsity constraint on the object derivative space for compressive holography. Together with spectrum domain zero-padding, our compressive algorithm allows for sub-pixel accuracy edge localization.

The extension to the 2D case is not trivial. It has been shown that the spiral phase mask can serve as an approximate 2D derivative operator in the Fourier domain. In this case, we implemented spiral phase filtering in the hologram spectrum domain. By applying cross-correlation between reconstructions for consecutive sub-pixel movements, sub-pixel movement was successfully detected.

Thesis Supervisor: George Barbastathis
Title: Professor

Acknowledgments

I would like to thank, first and foremost, my thesis advisor, Professor George Barbastathis. I came to MIT without any optics or electro-magnetics background. He has been warmly and patiently guiding me during the course of my research and giving me many helpful suggestions.

I would also like to thank all my colleges at the 3D Optical Systems group for all their help and many helpful discussions: Lei Tian, Chih-Hung Max Hsieh, Hanhong Gao, Justin Lee, Howard Yuanhao Huang, Jon Petruccelli, Yen-Sheng Lu, Yongjin Sung, Jeong-gil Kim, Hyungryul Johnny Choi, Nick Loomis, Se Baek Oh, Yuan Luo, Jason Ku, Shakil Rehman and so on. Especially, I would like to thank Lei Tian, Max Hsieh and Hanhong Gao for their many helps since I came here. They gave me much helpful guidance on optics, signal processing as well as my personal life.

Also, I would like to thank Professor Berthold Horn for his helpful suggestions for this thesis and Professor Michael S. Triantafyllou and Heather Beam, our collaborators for this project. In addition, I would like to thank our funding sources: the National Research Foundation (NRF) of Singapore through the Singapore-MIT Alliance for Research and Technology (SMART) Center for Environmental Sensing and Modeling (CENSAM), the Chevron Energy Technology Company. Finally, I would like to thank the Xerox company for offering me the Xerox MIT fellowship as well as my upcoming summer internship.

Finally, I would like to thank my parents for their ever-lasting love, support, and encouragement.

Contents

1	Introduction	11
1.1	Traditional point-to-point imaging	11
1.2	Introduction to digital holography	12
1.3	Outline of the thesis	15
2	Introduction to compressive sensing	17
2.1	Nyquist–Shannon sampling theorem	17
2.2	Compressive sensing	18
2.2.1	Sparsity	20
2.2.2	Incoherence	21
2.2.3	Examples of incoherent measurements	22
2.2.4	Number of required measurements for compressive reconstruction	24
2.2.5	Why ℓ_1 minimization?	25
3	One dimensional (1D) sub–pixel movement detection using compressive holography	27
3.1	Incoherence and sparsity in digital holography	28

3.2	Compressive holography	30
3.2.1	Theoretical model for compressive holography	30
3.2.2	Sparsity recovery from partial measurements	31
3.3	1D sub-pixel motion detection experimental setup	36
3.4	Experimental results for 1D sub-pixel motion detection	38
4	2D sub-pixel movement detection using spiral phase filtering and compressive holography	43
4.1	Spiral phase mask	45
4.1.1	Introduction to spiral phase mask	45
4.1.2	Edge detection via spiral phase mask	46
4.2	Implementing the spiral phase mask to 2D compressive holography model	48
4.3	Experimental setup for 2D sub-pixel movement detection	49
4.4	Experimental result for detecting 2D sub-pixel displacements	50
5	Conclusions and Future work	53

List of Figures

1-1	Traditional point-to-point imaging system.	12
1-2	Schematic of a lensless in-line DH setup.	13
3-1	(a) Vector representation of the 1D object; (b) The sparse derivative of the object.	28
3-2	In-line DH geometry. The object was moved along y direction with a uniform step size of 267nm(1/45-pixel) by a piezo-driven motion stage.	30
3-3	Experimental in-line DH setup. The pin object was moved along y direction with a uniform step size of 267nm(1/45-pixel) by a piezo- driven motion stage.	37
3-4	A sample 2D hologram.	38
3-5	A sample row vector from the 2D hologram in Figure 3-4.	39
3-6	Real part of the compressive reconstruction of the 1D hologram in Figure 3-5.	40

3-7	Compressive reconstructed positions of seven randomly chosen rows (in blue circles) and the “true” position (in red stair curve) at each step. The histogram on the bottom right combines the data of total 45 steps taken by the seven rows ($45 \times 7 = 315$ data points total.)	40
3-8	The comparison between the average position (purple points) of each step and the “true” positions.	41
4-1	(a) A square object; (b) the derivative of the square along the horizontal direction; (c) the 2D derivative of the square.	44
4-2	The phase distribution on the spiral phase mask.	45
4-3	Edge detection function of spiral phase mask.	47
4-4	A sample hologram of the shim object.	49
4-5	Reconstruction results of the shim’s edges via the compressive method (a) and traditional back-propagation method (b).	51
4-6	(a) Normalized cross-correlation result between two consecutive reconstructions; (b) Detected positions of the shim object at each step. . .	51

Chapter 1

Introduction

Motion detection is an important practical problem. Intuitively, it can be achieved by taking differences of consecutive images. The problem becomes complicated if the displacement of an object is much less than the pixel size of a detector. In traditional imaging, sub-pixel movement detection is difficult because the movement only affects the pixels around the geometrical image point. In contrast, digital holography could improve the ability to measure sub-pixel displacement because it records the diffraction pattern from the object, and the information of the movement spreads over the entire detector area. This thesis aims to show how to combine compressive sensing and digital holography to solve the sub-pixel movement detection problem.

1.1 Traditional point-to-point imaging

Figure 1-1 shows the schematic of traditional point-to-point imaging system. The magnification of the object is decided by the focal length of the convex lens as well

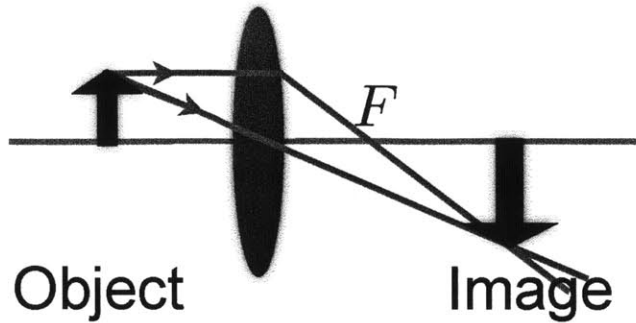


Figure 1-1: Traditional point-to-point imaging system.

as the distance between the object and the lens. However, no matter how the object is magnified, when the range of motion is smaller than the pixel size (after taking magnification not account), most of the information on the image will remain the same except for that around the edges of the object. As a result, if we desire to detect the sub-pixel movement of the object by capturing images of the object before and after the displacement through this traditional method, most of the content on the images are not useful for detecting the tiny movement. In other words, it is not efficient to extract sub-pixel movement by using traditional imaging techniques.

1.2 Introduction to digital holography

Digital holography (DH) is a famous technique for reconstructing a 3D profile of the object with only one single shot [1, 2, 3, 4, 5, 6, 7]. Digital holography and digital holographic image processing have become more applicable due to advances in mega-pixel electronic sensors, e.g. CCD and CMOS, with high spatial resolution and high dynamic range. DH has been widely used in two-phase flow imaging, phase contrast

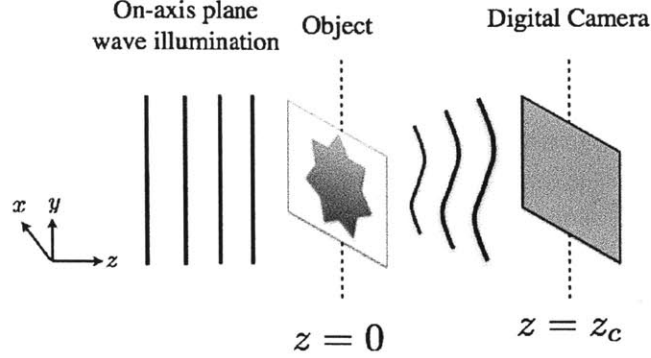


Figure 1-2: Schematic of a lensless in-line DH setup.

imaging and particle image velocimetry (PIV) [5, 8, 9].

There are mainly two different kinds of DH setup, in-line and off-axis. In our work, we only consider in-line lensless DH [10, 11, 5]. Figure 1-2 shows the schematic of a typical lensless in-line DH setup. Here, by “lensless”, we mean that there is no lens between the object and the digital detector.

When the plane wave illumination propagates onto the object, some of the light will be scattered by the object. In this simple in-line DH system, we assume that the scattering is not severe; in other words, most of the illumination remains unscattered after it propagates through the object. The light field propagates according to free-space (Fresnel) propagation between the object and the detector. At the detector plane, the unscattered part will serve as a reference wave, and interfere with the propagating object field.

The intensity of the interference pattern $I(m\Delta, n\Delta, z_D)$ recorded on the 2D de-

tector array can be written as

$$\begin{aligned}
I(m\Delta, n\Delta, z_D) &= |A_r + a(m\Delta, n\Delta, z_D)|^2 \\
&= A_r^2 + |a(m\Delta, n\Delta, z_D)|^2 + A_r a^*(m\Delta, n\Delta, z_D) + A_r^* a(m\Delta, n\Delta, z_D),
\end{aligned} \tag{1.1}$$

where Δ is the pixel size on the digital detector, A_r is the amplitude of the illumination plane wave, z_D is the distance between the object plane and detector plane, and $a(m\Delta, n\Delta, z_D)$ is the field of the scattered light at the recording plane. In Equation 1.1, the term A_r^2 is simply a constant and can be removed by eliminating the DC term when conducting Fourier transforming the interference pattern $I(m\Delta, n\Delta, z_D)$. Moreover, without loss of generality we may assume A_r as 1. The second term may be dropped as negligible when assuming $|a(m\Delta, n\Delta, z_D)| \ll A_r$. In line holography has an inherent limitation caused by the generation of overlapping twin images. Here the so-called twin image problem can be eliminated by using compressive reconstruction method as proposed in [12], which will be introduced in Chapter 2. According to the Huygens-Fresnel principle and the Fresnel approximation, the scattered field at $z = z_c$ can be expressed in the form

$$a(m\Delta, n\Delta, z_D) = g(m\Delta, n\Delta) * h(m\Delta, n\Delta), \tag{1.2}$$

where $*$ denotes the convolution operator and $h(m\Delta, n\Delta)$ is the free-space propagation point-spread-function $\exp\left(ik\sqrt{m^2\Delta^2 + n^2\Delta^2 + z_D^2}\right)$. Hence, by neglecting the

halo and twin-image terms in (1.1), the information encoded on the hologram has a linear relationship with the field at the object plane as

$$I(m\Delta, n\Delta, z_D) = g(m\Delta, n\Delta) * h(m\Delta, n\Delta) + e, \quad (1.3)$$

where e includes the halo, the twin image as well as other sources of noise that are uncorrelated to the object. Since there is a convolution operator in Equation 1.3, each measurement captured on the hologram contains the information of the whole object. In other words, all the measurements in this single shot during the holography experiment can contribute to detect sub-pixel movement, which means using digital holography can greatly increase the chance to detect the sub-pixel motion, as opposed to the traditional point-to-point imaging technique where the edge information is localized.

1.3 Outline of the thesis

Optical real-time detection of small motions enables progress in diverse scientific domains. Examples are observation of Brownian motion [13], tracking of a single molecule [14, 15, 16], etc. Of particular interest in our group is the measurement of small mechanical vibrations, which would allow the modeling of complex fluid-elastic interactions in seal whiskers [17, 18]. Intuitively, the accuracy (smallest detectable movement) is limited by the finite pixel size of the digital camera. Curve fitting methods [14, 16, 3] or feature-based tracking methods such as digital image correla-

tion [19, 20, 21] and gradient-based image registration [22, 23, 24] improve accuracy beyond the pixel limit, subject to noise limitations. Alternatively, scanning yields even more dramatic accuracy improvements [25, 26] at the cost of slower frame acquisition.

In Chapter 2, compressive sensing is introduced. The basic concept and properties of compressive sensing and the pre-requirement of compressive sensing are summarized. The sparsity and the so-called “incoherence” of the linear sensing system are very important in compressive sensing. Both of those two factors will affect the required number of measurements for accurate compressive reconstruction.

In Chapter 3, the incoherence and sparsity of in-line digital holography are discussed. The derivative operator is applied to sparsify the object function and a linear model is built for compressive holography. The number of measurements required for accurate reconstruction is studied. Experimental setup and results for 1D sub-pixel movement detection using compressive holography are presented. $1/45$ pixel size movement can be successfully detected.

In Chapter 4, the spiral phase mask is introduced to sparsity a general 2D object. Experimental setup and results for 2D sub-pixel movement detection are also shown.

In Chapter 5, conclusions of this thesis and directions for future research are presented.

Chapter 2

Introduction to compressive sensing

2.1 Nyquist–Shannon sampling theorem

The Nyquist–Shannon sampling theorem, named after Harry Nyquist and Claude Shannon, is a fundamental theorem in the field of information theory, especially in the area of signal processing and data acquisition. Sampling is the process of converting a continuous signal (for example, a function of continuous time or space) into a discrete sequence signal (a function of discrete time or space).

To maintain the ability to reconstruct the original continuous–time signal, for the sampled signal, the sampling strategy must meet certain criteria. For example, considering the continuous–time signal $\sin(\pi t)$, if we sample it when t is an integer, the resulting sampled signal will be all zeros, which will lead to a failed reconstruction.

This is a phenomenon called under–sampling.

According to Nyquist–Shannon sampling theorem, if a function $x(t)$ contains no frequencies higher than B Hz, then $x(t)$ may be entirely reconstructed from the samples if the sampling spacing is $1/2B$ sec or less. Equivalently, a band–limited analog signal with band–width of B can be perfectly reconstructed if we sample the signal with $2B$ sampling rate.

The theorem assumes an idealization of any real–world situation, as it only applies to signals that are infinitely long in the time space; However, in the real world all the signals are time–limited which cannot be perfectly band–limited. However, many signals of practical interest *approximately* meet both specifications, i.e. no significant amounts of energy are present either outside the frequency band B or the time duration T .

Recently, it has been shown that for an under–determined linear sampling system, the continuous analog signal can still be perfectly reconstructed if the input signal is sparse or compressible. This result is known as the compressive sensing theorem.

2.2 Compressive sensing

The basic idea of compressive sensing is that sparse signals can be accurately reconstructed from a small amount of linear measurements [27, 28, 29].

The acquisition of a signal x can be modeled as M linear measurements of x :

$$y_k = \langle \phi_k, x \rangle, k = 1, \dots, M. \quad (2.1)$$

Here we assume that x is a N -dimensional vector, so the dimension of x is $N \times 1$ and that ϕ is a $M \times N$ matrix. Solving for x from the measurements in y is a linear inverse problem. If $M = N$ and ϕ is a full rank matrix, which means that the measurements are all linearly independent, x can be obtained directly by $x = \phi^{-1} \cdot y$. If $M < N$, ϕ^{-1} does not exist and this linear system becomes under-determined. However, if the input signal is sparse in some pre-known basis and the measurements are taken randomly, the reconstruction of x is possible even if with measurements much fewer than N .

When saying x is sparse, we mean that in some known orthogonal basis ψ , x can be represented by a N -dimensional vector a with only s non-zero coefficients, where s is much smaller than N . In this way, x and y can be expressed as

$$x = \psi \cdot a, \tag{2.2}$$

$$y = \phi \cdot \psi \cdot a. \tag{2.3}$$

In order to recover the signal x , we can take advantage of the sparsity property and first reconstruct the sparse signal a . If the sparsifying basis ψ is known, it is straightforward to obtain x from a . Several papers have proved that by solving the $\|a\|_{\ell_1}$ minimization problem, a can be perfectly reconstructed as long as the measurements are noise-free. Given this system and all the m measurements in y , a can be recovered

by solving the ℓ_1 minimization problem

$$\hat{a} = \underset{a}{\operatorname{argmin}} \|a\|_{\ell_1}, \text{ such that } y = \phi \cdot \psi \cdot a. \quad (2.4)$$

Compressive sensing can be highly successful in solving the under-determined problem; however, to guarantee accurate stable reconstruction, there must be some constraint (or lower limit) on the number of measurements. The constraint here depends on the degree of sparsity of the input signal and an “incoherence” parameter μ , which measures the incoherence between the sensing matrix ϕ and the sparsifying basis ψ . We discuss the two constraints briefly in the next two sections.

2.2.1 Sparsity

If the signal has a sparse representation under the orthogonal basis ψ , one can discard some of the small coefficients without significant loss in reconstruction fidelity. Some image compression techniques also take advantage of this kind of eliminating small coefficients for compression. For example, in JPEG 2000 format, the image is transformed into a wavelet basis where the representation is sparser. Comparing to the JPEG technique which discards the high frequency content, the JPEG 2000 can keep the smooth regions on the original image with good fidelity while the edges become much sharper. Furthermore, the sparser the original signal a is, the fewer measurements are required to obtain accurate reconstruction.

2.2.2 Incoherence

The “incoherence” term measures how the information of the input signal, which has a sparse representation in ψ , spreads out in the sensing matrix ϕ . In other words, incoherence measures how the input signals mix in the measurements. The input signal is local, while the measurements are global as each of the measurements should contain some information about each component in the input signal. Let us take the Dirac function as an example. In the space domain, the Dirac function is just a spike, which is a very sparse signal, while in the Fourier domain, the signal turns to a very flat function with “1”s everywhere. This means that the information of the Dirac function spreads out onto the whole domain of the Fourier space.

With a sampling matrix that has been properly normalized by $A \cdot A^\dagger = NI$ or $\phi \cdot \psi \cdot (\phi \cdot \psi)^\dagger = NI$ where $I = \text{diag}(1)$ is the unit matrix, the coherence parameter can be computed by [27]

$$\mu(\phi, \psi) = \max_{1 \leq k, j \leq N} |\langle \phi_k, \psi_j \rangle|. \quad (2.5)$$

If we define $A \triangleq \phi \cdot \psi$ and $y = A \cdot a$, the coherence parameter can be also expressed as

$$\mu(A) = \max_{1 \leq k, j \leq N} |A_{kj}|. \quad (2.6)$$

From (2.5), we can see that the coherence parameter measures the correlation between the columns in ϕ and ψ . If some of columns in ϕ and ψ are correlated or dependent, the coherence parameter will be large. On the contrary, if the columns in ϕ and ψ are

totally independent, as is the case with Fourier sampling, the coherence parameter will reach its minimum value. Typically, μ is in the range of $[1, \sqrt{N}]$.

2.2.3 Examples of incoherent measurements

- Discrete Fourier Transform (DFT)

For N -dimensional DFT matrix W , the transformation matrix w is of the form

$$W = \begin{bmatrix} 1 & 1 & 1 & 1 & \dots & 1 \\ 1 & w & w^2 & w^3 & \dots & w^{N-1} \\ 1 & w^2 & w^4 & w^6 & \dots & w^{2(N-1)} \\ 1 & w^3 & w^6 & w^9 & \dots & w^{3(N-1)} \\ \vdots & \vdots & \vdots & \vdots & \ddots & \vdots \\ 1 & w^{N-1} & w^{2(N-1)} & w^{3(N-1)} & \dots & w^{(N-1)(N-1)} \end{bmatrix},$$

where $w = e^{-\frac{i2\pi}{N}}$. It is clear that the discrete Fourier transform matrix W satisfies the normalization rule $W \cdot W^\dagger = NI$. Then we can randomly sample the Fourier coefficients of the input signal. By calculating the coherence parameter for this sensing matrix W , it is easy to see that $\max_{1 \leq k, j \leq N} |W_{kj}|$ is 1. So for the complex Fourier sampling matrix, its coherence parameter μ is 1 the lowest limit the coherence parameter may attain.

- Identity Matrix

When the sensing matrix is just a magnified identity matrix $\sqrt{N}I$, we can predict that this sensing system has the largest coherence parameter. Consid-

ering a signal x in the space domain, if we randomly sample x directly, then $y = \sqrt{N}I \cdot x$. As identity matrix is the same as the space domain coordinate, in this case, ϕ is the same as ψ , which means these two matrices are coherent to the maximum extent. In the language of compressive sensing, this kind of sampling is the least efficient sampling. By calculating the coherence parameter from (2.6), we can also obtaine μ as \sqrt{N} , which matches with our prediction.

- Random convolution

Convolution is the general implementation of a linear shift-invariant system. Suppose $y = h * x$, using Fourier-domain multiplication instead of direct convolution, we obtain in matrix form

$$y = W^\dagger \cdot \hat{h} \cdot W \cdot x, \tag{2.7}$$

where W and W^\dagger denote the Fourier transform and inverse Fourier transform respectively, and \hat{h} is the Fourier transform of h . In (2.7), the h matrix is diagonal and its entries along the diagonal are the Fourier coefficients of the convolution kernel h .

If the magnitude of all the entries along the diagonal of \hat{h} are the same, \hat{h} can be normalized by a scalar factor so that the sensing matrix in the Equation 2.7 satisfies the normalization rule $A \cdot A^\dagger = NI$. In this case, A is just $W^\dagger \cdot \hat{h} \cdot W$. If the magnitudes are not the same, it does not quite satisfy the pre-requirement of compressive sensing. This case is beyond the scope of this work.

2.2.4 Number of required measurements for compressive reconstruction

Suppose that the fixed sparse representation of the signal x in the orthogonal basis ψ is s -sparse. Select M uniformly random measurements from the ϕ domain. It is shown that if [27]

$$M \leq C \cdot \mu^2 \cdot S \cdot \log(N), \quad (2.8)$$

where C is a small positive constant, the signal x can be reconstructed exactly with high probability. It has been shown that the probability of successful reconstruction will exceed $1 - \delta$ when $M \leq C \cdot \mu^2 \cdot S \cdot \log(N/\delta)$.

From (2.8), it is clear that the number of measurements should be proportional to the coherence parameter and the degree of sparsity. As mentioned above, the more incoherent the sensing matrix is with respect to the orthogonal sparsifying matrix, the more mixing of the input signal the measurements will incur, which equivalently means fewer measurements are required to guarantee exact recovery. Another important point is that the more sparse the signal is, the fewer measurements it requires to reconstruct the signal x . These are the reasons why coherence and sparsity are two important factors for judging whether the sensing system and input signal are good to use compressive reconstruction.

2.2.5 Why ℓ_1 minimization?

For a N -dimensional vector u , its ℓ_p norm can be expressed as

$$\|u\|_p = \sum_{j=1}^{j=N} |u_j|^p. \quad (2.9)$$

In most works on signal recovery or signal denoising, ℓ_2 minimization, also known as minimum square error approach is widely used. The ℓ_2 norm corresponds to the total energy of a signal. It has been popular for denoising, in the sense of minimizing the energy in the difference between the recovered signal and the actual input signal. But why in compressive sensing do we choose ℓ_1 norm, rather than ℓ_2 norm?

Before thinking about this question in a mathematical way, let us solve a simple problem first ¹. In a farm, the farmer raised some chickens and sheep. The farmer told us that the total number of the animals' legs is 16. Now the question becomes how many chickens and sheep respectively are in the farm. This is definitely an under-determined problem as we are supposed to solve two unknowns with only one equation:

$$2x + 4y = 16, \quad (2.10)$$

where x denotes the number of chickens and y denotes that of sheep. If the farmer tells us another constraint on the solution that the ℓ_1 norm of the solution should be minimized, the solution can be immediately obtained as $x = 0, y = 4$, which is also a so-called sparse solution (only one entry of the solution is non-zero). However, if

¹This example was constructed by Justin W. Lee

the solution's ℓ_2 norm of the solution should be minimized, the answer will change to $x = 2, y = 3$. We can see that the solution that minimizes the ℓ_2 norm are not sparse at all, instead, it decreases the value of y at the cost of sparsity.

From the perspective of maths, in a three-dimensional Cartesian coordinate, all the sparse signals fall mostly on the axes. Points with the same ℓ_1 norm form a diamond-shape surface with the diamond corner located on the axes, while those with the same ℓ_2 norm form an ellipsoidal surface. When the size of the diamond or ellipsoid expands, the ℓ_1 norm or the ℓ_2 norm respectively become large. The minimum error solution is found on the point of intersection of the error surface with the surface expressing the solution constraint (e.g. $2x + 4y = 16$ in the farmer's example above). If the error surface is ellipse (ℓ_2 case), it can intersect the solution constraint; whereas if the error surface is diamond-shape (ℓ_1 case) then it is more directly to intersect the solution constraint on one of the axes, thus yielding a "sparse" solution. ² Thus, by solving the ℓ_1 norm minimization problem, we are inclined to get a sparse solution.

Here we only compare the two methods, ℓ_1 norm minimization and ℓ_2 norm minimization. However, ℓ_1 norm minimization is not the only way to reconstruct sparse signals; some other methods have also been proposed.

²This geometrical explanation was provided by Lei Tian

Chapter 3

One dimensional (1D) sub-pixel movement detection using compressive holography

In our work, we investigate the problem of scanning-free small motion detection from a sampling perspective.

As shown in Chapter 1, in the DH setup, the hologram is captured on a digital camera with finite pixel size, which limits the rate at which the intensity signal is sampled. In the real world, all objects are finite, which means that the frequency response of a object is infinite. In this way, it is impossible to apply Nyquist theorem to sample the signal and then perfectly reconstruct the input signal. Nyquist theorem, however, does not take into account any *prior* information about the object. It has been shown in Chapter 2 that using compressive sensing, a sparsity-based

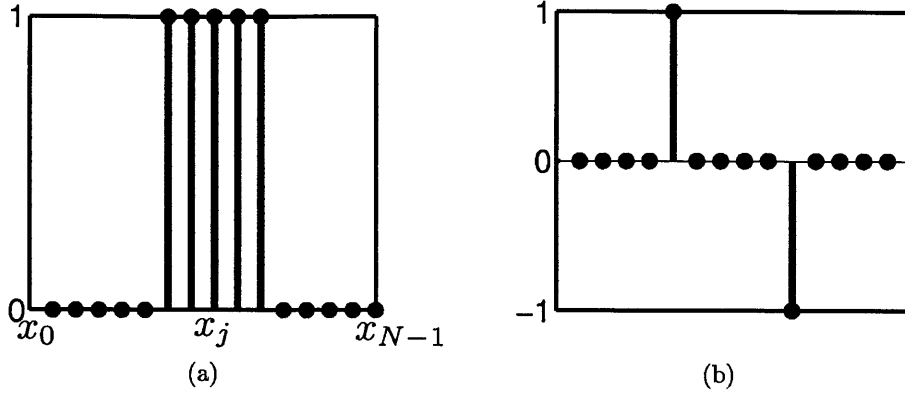


Figure 3-1: (a) Vector representation of the 1D object; (b) The sparse derivative of the object.

sampling theory, highly accurate solutions of an under-sampled linear system can be obtained [30, 29]. In addition, the solution is robust to noise [31].

3.1 Incoherence and sparsity in digital holography

As mentioned in Chapter 2, successful implementation of compressive reconstruction is conditioned upon two requirements: sparsity and incoherence [28]. To enforce sparsity of the object signal, we consider a one-dimensional (1D) signal, as illustrated in Figure 3-1(a).

Let us define a coordinate vector

$$\mathbf{x} = [x_0, x_1, \dots, x_j, \dots, x_{N-1}], \quad (3.1)$$

where $x_n = nd$; $n = 0, 1, \dots, N - 1$; and d denotes the desired motion accuracy.

The pixel size is $\Delta = Gd$, where G is our intended sub-pixel accuracy gain of mo-

tion detection. We will consider only a single opaque object surrounded by uniform intensity within the field of view; the intensity at the object plane may therefore be represented as a vector \mathbf{I}^{obj} of length N corresponding to the coordinate vector \mathbf{x} , where

$$\mathbf{I}^{\text{obj}} = [0, \dots, 0, 1, \dots, 1, 0, \dots, 0]. \quad (3.2)$$

Fig. 3-1(a) shows \mathbf{I}^{obj} from one such possible object. The vector \mathbf{I}^{obj} is unknown in the sense that we do not know where the transitions between value 1 and value 0 occur. This vector is not sparse, but we can easily sparsify it by taking the spatial derivative along x , which will produce two impulses at the edges of the object. Then, the new sparse derivative vector is in the form of

$$\Delta\mathbf{I}^{\text{obj}} = [0, \dots, 0, 1, 0, \dots, 0, -1, 0, \dots, 0], \quad (3.3)$$

and what is unknown is the locations of the impulses.

The second requirement about “incoherence” does not use the term according to the typical sense we assign in Statistical Optics; rather, it means that the information of the unknown vector $\Delta\mathbf{I}^{\text{obj}}$ must be evenly spread over the set of basis vectors that describe it [28]. We utilize diffraction for that purpose, which is what motivated our use of Fresnel holography [12, 32]. The spreading produced by the Fresnel propagator is not provably optimal, but it is extremely easy to attain by simple free-space propagation in the lab. To implement the optimal operator, one would require special-purpose phase masks placed at certain locations along the path; that

is beyond the scope of the present work.

3.2 Compressive holography

3.2.1 Theoretical model for compressive holography

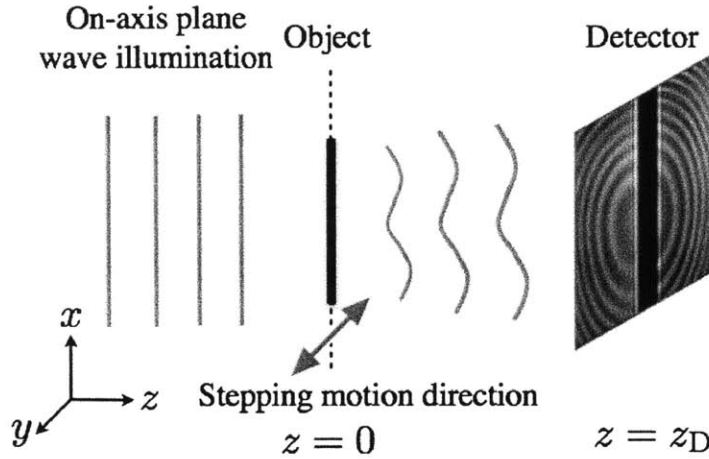


Figure 3-2: In-line DH geometry. The object was moved along y direction with a uniform step size of 267nm(1/45-pixel) by a piezo-driven motion stage.

Figure 4-2 is a schematic of a typical in-line digital holography setup. A linear model has been obtained in Equation 1.3 as

$$I(m\Delta, n\Delta, z_D) = g(m\Delta, n\Delta) * h(m\Delta, n\Delta) + e, \quad (3.4)$$

where Δ is the pixel pitch on the digital detector and e includes the halo, the twin image as well as other sources of noise that are uncorrelated to the object.

We multiply the Fourier transform of the intensity by iu , where u is the spatial frequency variable, to obtain the derivative in the spatial domain. To upsample so

that we can measure sub-pixel movement, the spectrum of the hologram is then zero-padded at both sides. Finally, a linear model relating the derivative of the object g' and the hologram I expressed in the Fourier domain can be obtained in the form of

$$iu \cdot \mathcal{F} \cdot I = Q \cdot (H \cdot \mathcal{F} \cdot g' + iu \cdot e'), \quad (3.5)$$

where \mathcal{F} denotes the discrete Fourier transform matrix, H is a diagonal matrix with the Fourier transform of h at the diagonals, and e' is the Fourier-transformed noise. The mask Q in Equation 3.5 is a diagonal matrix with $[0, \dots, 0, 1, 1, \dots, 1, 0, \dots, 0]$ along its diagonal and the total number of 1 in Q 's diagonal is M , which is also the number of pixels in the recorded hologram. Since the edges of the object are sparse, (3.5) can be inverted by enforcing the sparsity constraint using ℓ_1 -minimization. The edges (derivative) $\widehat{g'}$ of the object can be estimated by solving

$$\begin{aligned} \widehat{g'} &= \underset{g'}{\operatorname{argmin}} \|g'\|_{\ell_1}, \text{ such that} \\ iu \cdot \mathcal{F} \cdot I &= Q \cdot H \cdot \mathcal{F} \cdot g', \end{aligned} \quad (3.6)$$

where $\|\cdot\|_{\ell_1}$ denotes the ℓ_1 -norm of a vector. We implemented ℓ_1 -minimization by adapting the Two-step Iterative Shrinkage/Thresholding (TwIST) algorithm [33].

3.2.2 Sparsity recovery from partial measurements

Let s denote the ‘‘sparsity’’ of the problem, *i.e.* the number of non-zero entries in the input signal. To accurately reconstruct an s -sparse vector x of length N , the number

of samples M should satisfy [27]

$$M \geq C\mu^2 s \log N, \quad (3.7)$$

where C is a small positive constant, and μ is the coherence parameter, which measures the correlation between the measurement matrix and the sparsifying basis. In our compressive holography model in (3.6), M is the number of pixels in the recorded hologram; N is the number of pixels after the compressive reconstruction, increased from M by zero-padding in the Fourier domain.

Intuitively in (3.7), the relationship between M and the other parameters μ, s, N , makes sense as it is straight-forward that the less sparse the input signal is, the more measurements the system requires to get the same probability of accurate recovery. As to μ and N , when the dimension of the input signal increases or when the sensing matrix is more coherent with respect to the sparsifying basis, both of these two cases will lead to smaller probability of accurate reconstruction if the number of measurements is kept the same.

Next, let us calculate the coherence parameter in our compressive holography model. As a digital camera is used in recording hologram, the sensing system in our system can be equivalently written in the form of:

$$I_{g'} = S \cdot \mathcal{F}^{-1} \cdot H \cdot \mathcal{F} \cdot g', \quad (3.8)$$

where $I_{g'}$ is the hologram of the object's edges g' . The dimension of $I_{g'}$ is the same as

the number of pixels on the detector (in our case, it is M), while g' is a N dimensional vector. S , in the form of

$$\begin{bmatrix} 1 & \dots & 1 & 1 & 0 & 0 & \dots & \dots & \dots & \dots & \dots & 0 & 0 \\ 0 & \dots & 0 & 0 & 1 & \dots & 1 & 1 & 0 & \dots & \dots & 0 & 0 \\ \vdots & \vdots & & & \vdots & & \vdots & & & & & \vdots & \vdots \\ 0 & 0 & \dots & \dots & \dots & \dots & \dots & 0 & 0 & 1 & \dots & 1 & 1 \end{bmatrix},$$

denotes the way the CCD converts the incoming photons into electron charges and then into intensity values on the hologram. The number of 1's in each row of S is G , corresponding to the gain factor in our sub-pixel motion detection system. As a result, the dimension of S is $M \times N$.

From Equation 3.8, the sensing matrix in the compressive holography system can be expressed as

$$A = S \cdot \mathcal{F}^{-1} \cdot H \cdot \mathcal{F}. \quad (3.9)$$

As described in [27], for an orthogonal matrix A with $A^\dagger A = NI$ where \dagger denotes the conjugate transpose of A , the coherence parameter $\mu(A)$ is simply the largest magnitude among the entries in A :

$$\mu(A) = \max_{k,j} |A_{k,j}|. \quad (3.10)$$

To normalize the sensing matrix A so that A satisfies $A^\dagger A = NI$, S should be

magnified by a scaling factor of \sqrt{M} . After normalization, S becomes

$$S = \sqrt{M} \begin{bmatrix} 1 & \dots & 1 & 1 & 0 & 0 & \dots & \dots & \dots & \dots & \dots & 0 & 0 \\ 0 & \dots & 0 & 0 & 1 & \dots & 1 & 1 & 0 & \dots & \dots & 0 & 0 \\ \vdots & \vdots & & & \vdots & & \vdots & & & & & \vdots & \vdots \\ 0 & 0 & \dots & \dots & \dots & \dots & \dots & 0 & 0 & 1 & \dots & 1 & 1 \end{bmatrix}.$$

Recall that the Fourier transform \mathcal{F} is expressed in matrix form as

$$F = \frac{1}{\sqrt{N}} \begin{bmatrix} 1 & 1 & 1 & 1 & \dots & 1 \\ 1 & w & w^2 & w^3 & \dots & w^{N-1} \\ 1 & w^2 & w^4 & w^6 & \dots & w^{2(N-1)} \\ 1 & w^3 & w^6 & w^9 & \dots & w^{3(N-1)} \\ \vdots & \vdots & \vdots & \vdots & \ddots & \vdots \\ 1 & w^{N-1} & w^{2(N-1)} & w^{3(N-1)} & \dots & w^{(N-1)(N-1)} \end{bmatrix},$$

where $w = e^{-\frac{i2\pi}{N}}$. Equivalently, $\mathcal{F}_{p,q}$ can be written as

$$\mathcal{F}_{p,q} = \frac{1}{\sqrt{N}} e^{-\frac{i2\pi}{N}(p-1)(q-1)}, \quad (3.11)$$

where $p, q = 1, \dots, N$. H , the Fourier Transform of Fresnel kernel, is

$$\begin{bmatrix} 1 & 0 & 0 & \dots & 0 \\ 0 & e^{i\pi \frac{\lambda z_D}{(M\Delta)^2}} & 0 & \dots & 0 \\ \vdots & \vdots & \vdots & \ddots & \vdots \\ 0 & \dots & 0 & e^{i\pi \frac{\lambda z_D}{(M\Delta)^2} \cdot (N-2)^2} & 0 \\ 0 & 0 & \dots & 0 & e^{i\pi \frac{\lambda z_D}{(M\Delta)^2} \cdot (N-1)^2} \end{bmatrix}.$$

Usually, there is a scaling factor involved. However, in our case, we can get rid of it when normalizing the sensing matrix A .

Define $B \triangleq \mathcal{F}^{-1} \cdot H \cdot \mathcal{F}$. From Einstein notation [34], the entries in B can be calculated as

$$\begin{aligned} B_{j,k} &= \frac{1}{N} \sum_{r=1}^N e^{\frac{i2\pi}{N}(j-1)(r-1)} \cdot e^{i\pi \frac{\lambda z_D}{(M\Delta)^2} \cdot (r-1)^2} \cdot e^{-\frac{i2\pi}{N}(r-1)(k-1)} \\ &= \frac{1}{N} \sum_{r=0}^{N-1} e^{i\pi \frac{\lambda z_D}{(M\Delta)^2} \cdot r^2} \cdot e^{-\frac{i2\pi}{N}r(k-j)} \\ &= \frac{M\Delta}{N\sqrt{\lambda z_D}} e^{-i \frac{(M\Delta)^2}{\lambda z_D} (k-j)^2} \\ &= \frac{\Delta}{G\sqrt{\lambda z_D}} e^{-i \frac{(M\Delta)^2}{\lambda z_D} (k-j)^2} \end{aligned} \quad (3.12)$$

where $j, k = 1, \dots, N$. As a result,

$$\begin{aligned} A_{v,t} &= \sum_{r=1}^N S_{v,r} B_{r,t} \\ &= \sum_{r=vG+1}^{(v+1)G} \frac{\Delta\sqrt{M}}{G\sqrt{\lambda z_D}} e^{-i \frac{(M\Delta)^2}{\lambda z_D} (t-r)^2}. \end{aligned} \quad (3.13)$$

Combining with (3.10), the coherence of the compressive holography system can finally be computed as

$$\mu(A) = \max_{v,t} |A_{v,t}| = \Delta \sqrt{\frac{M}{\lambda z_D}}. \quad (3.14)$$

According to (3.7) and (3.14), the sampling gain G has an upper bound:

$$G = \frac{N}{M} \leq \frac{1}{M} \exp\left(\frac{\lambda z_D}{C_s \Delta^2}\right). \quad (3.15)$$

The smallest detectable sub-pixel movement d_{\min} is then limited by the smallest pixel size after compressive reconstruction (corresponding to the maximum sampling gain G_{\max})

$$d_{\min} = \frac{\Delta}{G_{\max}} = \frac{M\Delta}{\exp\left(\frac{\lambda z_D}{C_s \Delta^2}\right)}. \quad (3.16)$$

3.3 1D sub-pixel motion detection experimental setup

Our lensless experimental setup for the 1D sub-pixel motion detection is shown in Figure 3-3. Here, “lensless” means there is no lens between the pin object and the digital camera. A collimated He-Ne laser of wavelength 632.8nm was used to illuminate the object. The input laser beam was expanded by a spatial filter, and collimated by a plano-convex lens. After propagating through the object, the resultant hologram

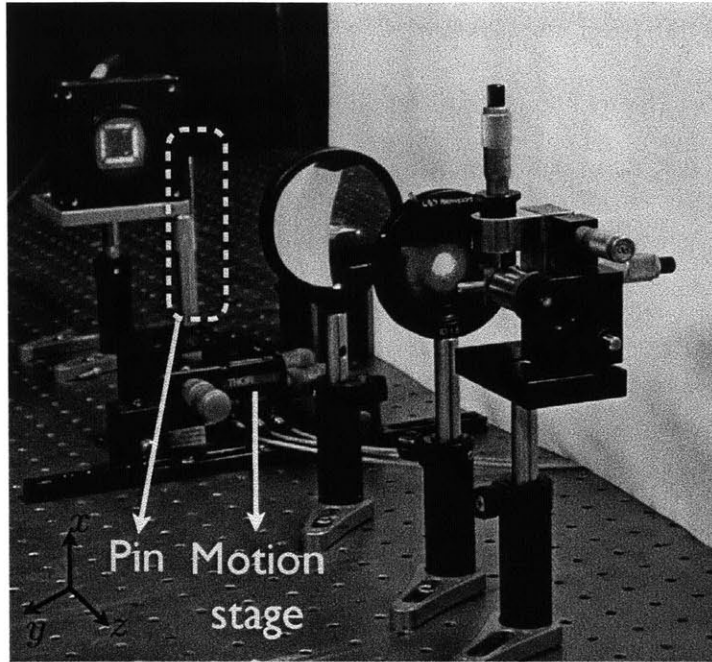


Figure 3-3: Experimental in-line DH setup. The pin object was moved along y direction with a uniform step size of 267nm ($1/45$ -pixel) by a piezo-driven motion stage.

was recorded by a Basler A504k camera with 1024×1024 pixels and $12\mu\text{m}$ pixel pitch. The object, a pin with an average diameter of $900\mu\text{m}$, was placed 151.6mm away from the detector. A piezo-driven motion stage (Model number: Thorlabs Nanomax 312) with 20nm resolution was used to move the pin laterally along the y direction step by step.

In the experiment, the pin object was modeled as a 1D rectangular function. This is well justified since the width of most part of the pin is uniform. Using our simulation, we found that $C \approx 30$ guarantees the reconstructed object position to be correct more than 50% of the time under our experiment conditions. Using this value of C in Equation (3.15), the maximum sampling gain G_{max} is found to be 60, which implies that the theoretically smallest detectable movement in our experimental

arrangement is 1/60-pixel size (200nm).

We verified our theory by moving the pin object along the y -axis with a step size of 267nm (equivalently 1/45-pixel size or gain of $G = 45$). The pin was moved by 45 steps (1 pixel) in total. A hologram was captured after each step of movement; a sample hologram is shown in Figure 3-4. A row vector of length 1024 can be extracted from the 2D hologram in Figure 3-4 to form a 1D hologram, as shown in Figure 3-5.

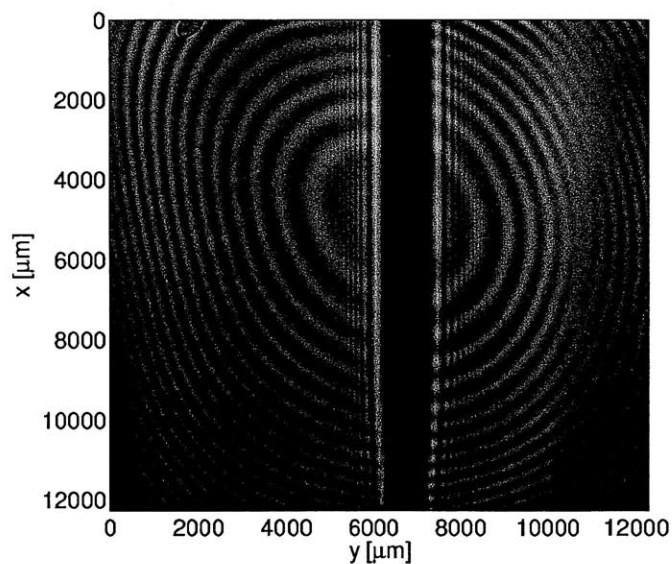


Figure 3-4: A sample 2D hologram.

3.4 Experimental results for 1D sub-pixel motion detection

The compressive reconstruction result of the 1D hologram in Figure 3-5 is shown in Figure 3-6. The edges of the original pin object were successfully reconstructed, free

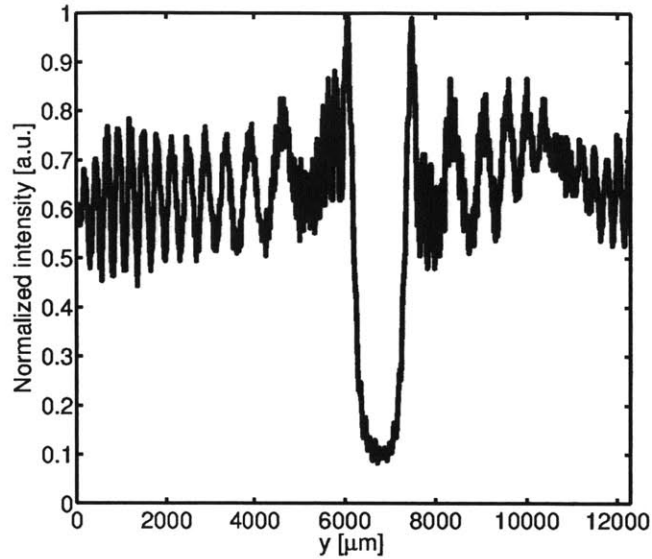


Figure 3-5: A sample row vector from the 2D hologram in Figure 3-4.

from artifacts due to twin image and other sources of noise.

To quantify the accuracy of our approach, we randomly chose seven rows (away from the pin’s tapered portion) from the first hologram (which defines the origin of pin’s movement), and then tracked the left edges of those seven rows for the following 45 steps. The compressive reconstruction was repeated for the same seven rows on the consecutive 45 holograms. Figure 3-7 shows the measured left edge positions of those seven rows from the total 46 holograms, compared with the “true” positions specified by the piezo stage. From the histogram shown on the bottom right in Figure 3-7, the average step size and precision (standard deviation) were calculated as 269nm and 12nm, respectively. The fraction of correct position reconstructions, *i.e.* those falling precisely on the 267nm mark, is 58%. It is also encouraging that less than 7% of the data are off by more than 1 step compared to the “true” position.

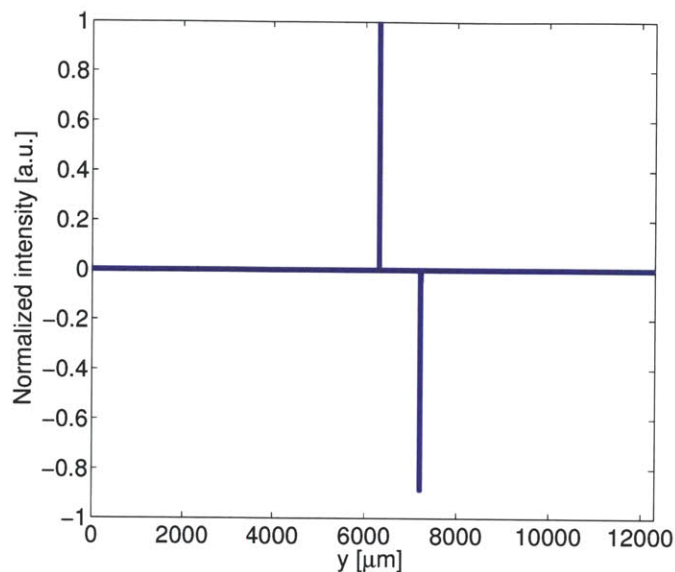


Figure 3-6: Real part of the compressive reconstruction of the 1D hologram in Figure 3-5.

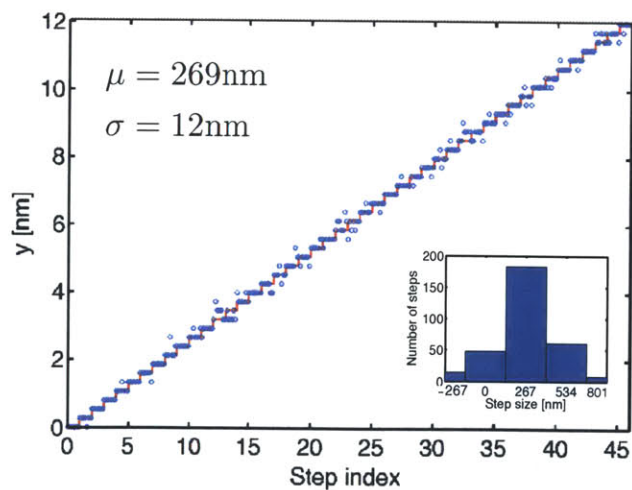


Figure 3-7: Compressive reconstructed positions of seven randomly chosen rows (in blue circles) and the “true” position (in red stair curve) at each step. The histogram on the bottom right combines the data of total 45 steps taken by the seven rows ($45 \times 7 = 315$ data points total.)

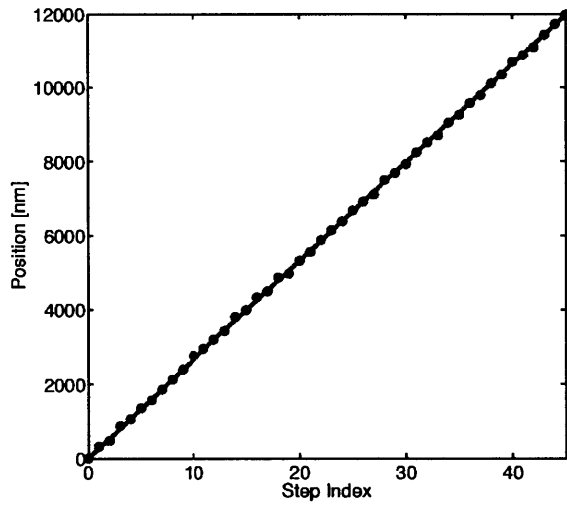


Figure 3-8: The comparison between the average position (purple points) of each step and the “true” positions.

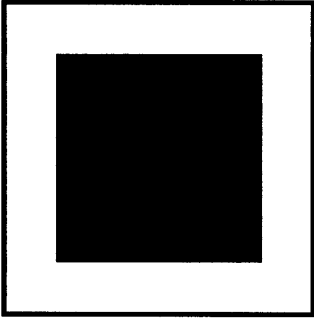
Chapter 4

2D sub-pixel movement detection using spiral phase filtering and compressive holography

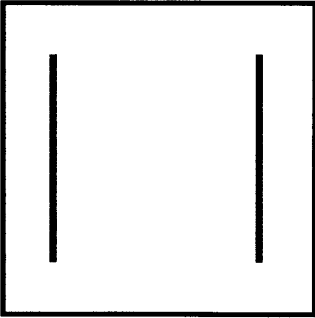
With the success of implementing compressive holography into detecting 1D sub-pixel movements, developing an algorithm to detect the sub-pixel movement in 2D is the natural next topic. However, it is not trivial to extend the 1D algorithm to 2D case, because the method we used to estimate the 1D derivative does not generalize to higher dimensions. Alternatively, we can think of the derivative as a Hilbert transform; which does not exist in 2D either.

Consider for example a square object (shown in Figure 4-1(a)). Its 1D derivative along the horizontal direction is a two-stripe function and the 2D derivative will be four points, corresponding to the four corners of the square. Apparently the four

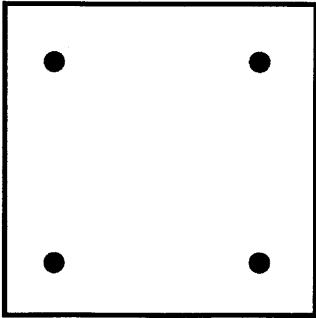
points extracted from the square by taking its 2D derivative are not the edges of the square, thus we are deprived of much valuable information about the object, completely missing its edges and being left with information about its corners only. Clearly, that ought not to be enough to localize sub-pixel motion for this square object.



(a)



(b)



(c)

Figure 4-1: (a) A square object; (b) the derivative of the square along the horizontal direction; (c) the 2D derivative of the square.

4.1 Spiral phase mask

4.1.1 Introduction to spiral phase mask

Spiral phase masks have been widely used in phase contrast microscopy [35, 36, 37, 38]. Usually under the microscope, biologists use them to observe some delicate structures in cells. The mask is a vortex filter, in the form of $\exp(i\phi)$, implemented in the Fourier domain of the image field. Here ϕ stands for the polar angular coordinate in the Fourier domain. The “stair-case” phase distribution on the spiral phase mask is shown in Figure 4-2.

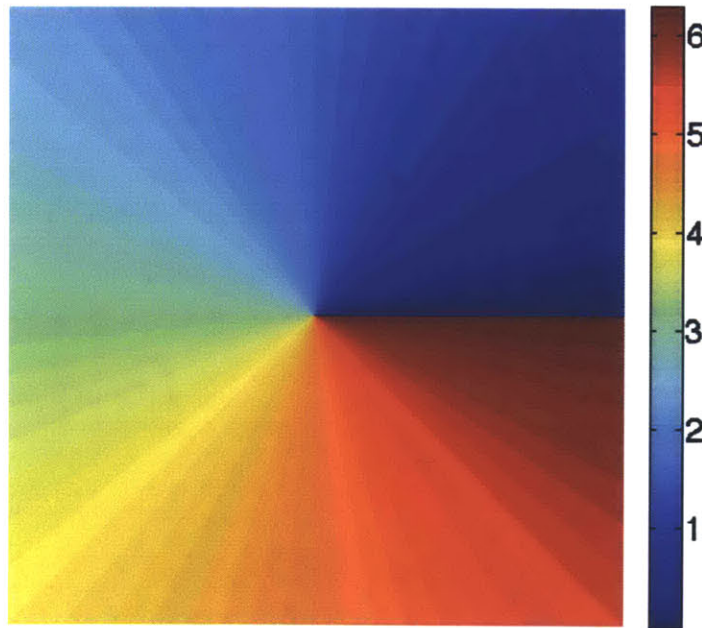


Figure 4-2: The phase distribution on the spiral phase mask.

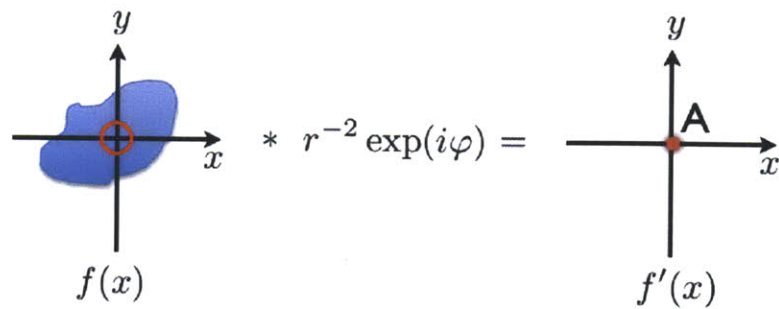
Unlike the dark field microscope, where the zeroth order of the illumination beam is blocked such that most of the intensity is lost, the spiral phase mask acts by redistributing while preserving the edges of the structures in the specimen. As a

result, spiral phase mask is very useful for edge detection.

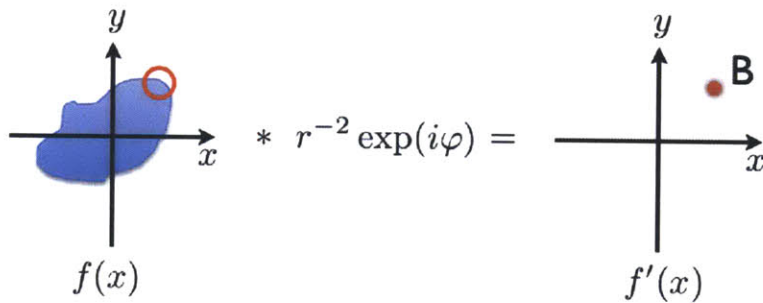
4.1.2 Edge detection via spiral phase mask

In the earlier experiments [39], spiral phase mask was introduced as an approximation to a two-dimensional Hilbert transform. When implementing such a spiral phase in the Fourier domain, equivalently the object is convolved with the Fourier transform of the phase mask function in the spatial domain. The Fourier transform of spiral phase mask can be expressed as $\frac{1}{r^2} \exp(i\varphi)$ [38], where r and φ are the polar coordinates in the object plane.

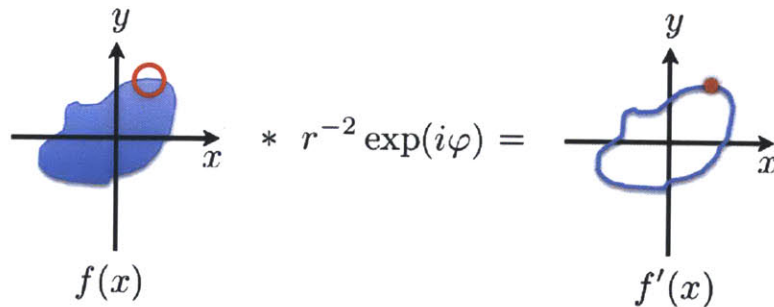
Figure 4-3 shows the convolution between a general 2D object function $f(x)$ with the Fourier transform. If all the points on the red ring denoted on the object, as in Figure 4-3(a), have the same values, in the convolution integral their total contribution to the original point on the convolution result, $f'(x)$, is zero, because all the points in the ring, their “ r ”s are the same and the φ of those points evenly distribute in the range of $[0, 2\pi]$. As a result, the value of point A on $f'(x)$ is zero. On the contrary, when the red ring overlaps the object’s edge, as shown in Figure 4-3(b), the values of some points on the rings are different from other points and thus, their total contribution to point B on $f'(x)$ will be non-zero.



(a)



(b)



(c)

Figure 4-3: Edge detection function of spiral phase mask.

By comparing the two cases in Figure 4-3(a) and (b), the edge detection function of the spiral phase mask can be clearly understood. Another important point is that since the Fourier transform of the spiral phase mask function is inversely proportional to the distance r , the mask is good for detecting local edges. In other words, spiral phase mask can be applied to edge detection, even for detecting the edges of a phase

object.

4.2 Implementing the spiral phase mask to 2D compressive holography model

In typical implementation of the spiral phase microscope, the Fourier filter is displayed at a high-resolution spatial light modulator (SLM) as a blazed phase hologram. In some other cases, researchers use a static phase hologram or a physical spiral phase plate instead of the spatial light modulator. In our work, we applied the spiral phase mask digitally to the spectrum of the hologram recorded by the CCD in the experimental digital holography setup. Ideally, via this multiplication, the spectrum of object's hologram can be directly converted to the spectrum of the object's edges' hologram.

After applying the spiral phase mask, the linear model relating the edge of the object g' and the measured hologram I expressed in the Fourier domain is

$$S \cdot \mathcal{F} \cdot I = Q \cdot H \cdot \mathcal{F} \cdot g', \quad (4.1)$$

where S denotes the spiral phase mask function $\exp(i\phi)$. Since the edge is a sparse representation of the original object, (4.1) can be inverted by minimizing the ℓ_1 -norm of g' . We implemented ℓ_1 minimization by adapting the Two-step Iterative Shrinkage/Thresholding (TwIST) algorithm [33]. (Details about this linear model were shown in Chapter 3.)

4.3 Experimental setup for 2D sub-pixel movement detection

We used an in-line digital holography arrangement to test the proposed method. A He-Ne laser of wavelength 632.8nm was used to illuminate the object. Holograms were taken by a Basler A504k camera. The object chosen for 2D sub-pixel motion detection was a stainless steel shim of inner diameter 2.24mm and outer diameter 3.88mm. The shim was attached to a three-axis piezo motion stage by a pin of diameter 250 μ m. The object was moved by six steps, and the step size was 3 μ m (equivalently 1/4 pixel size) in both horizontal and vertical directions. A hologram was captured after each step of movement. A sample hologram is shown in Figure 4-4.

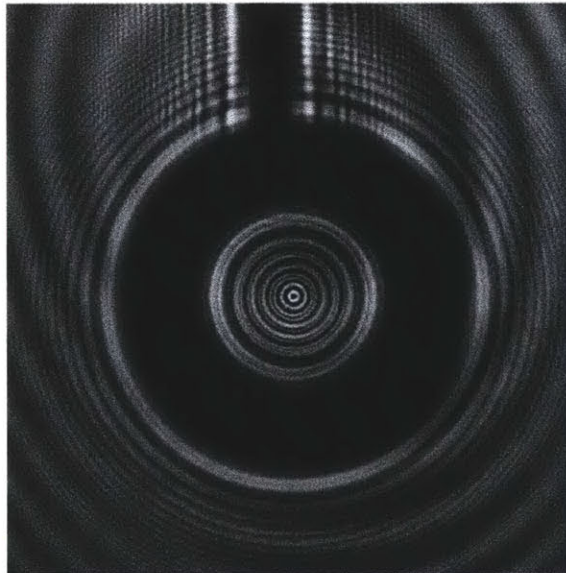


Figure 4-4: A sample hologram of the shim object.

4.4 Experimental result for detecting 2D sub-pixel displacements

To process the hologram at each step, the spectrum of the hologram was first zero-padded to four times its original size. After spiral phase mask filtering, Equation 4.1 was inverted using the TwIST algorithm. The compressive reconstruction result of the sample hologram is shown in Figure 4-5(a). By comparing the compressive reconstruction result with the traditional back-propagation reconstruction method shown in Figure 4-5(b), we can clearly see that the edges of the original object were successfully reconstructed, free from artifacts due to twin image and other sources of noise.

The compressive reconstruction was repeated for holograms after each movement. To extract the amount of movement, we computed the cross-correlation between the two consecutive reconstructions, identifying the relative movement of the object as equal to the displacement of the correlation peak. A sample cross-correlation is shown in Figure 4-6(a). The peak position indicates that in this single step, the object was moved by $3\mu\text{m}$ along the negative x direction and positive y direction respectively. The detected amount of movements for all the six steps are shown in Figure 4-6(b). The reconstructed location match perfectly with a straight line, proving the success of our model.

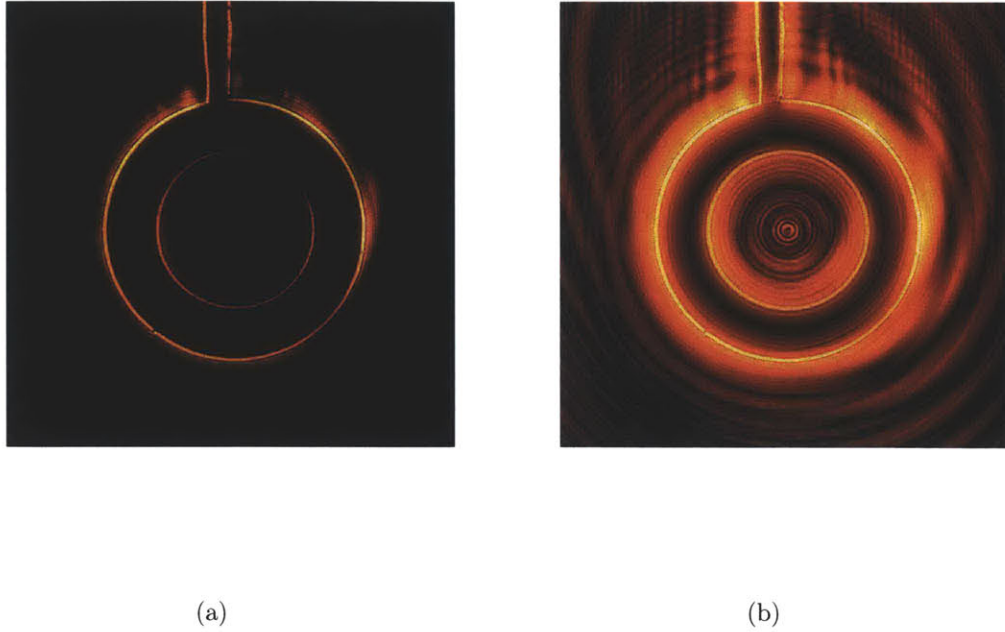


Figure 4-5: Reconstruction results of the shim's edges via the compressive method (a) and traditional back-propagation method (b).

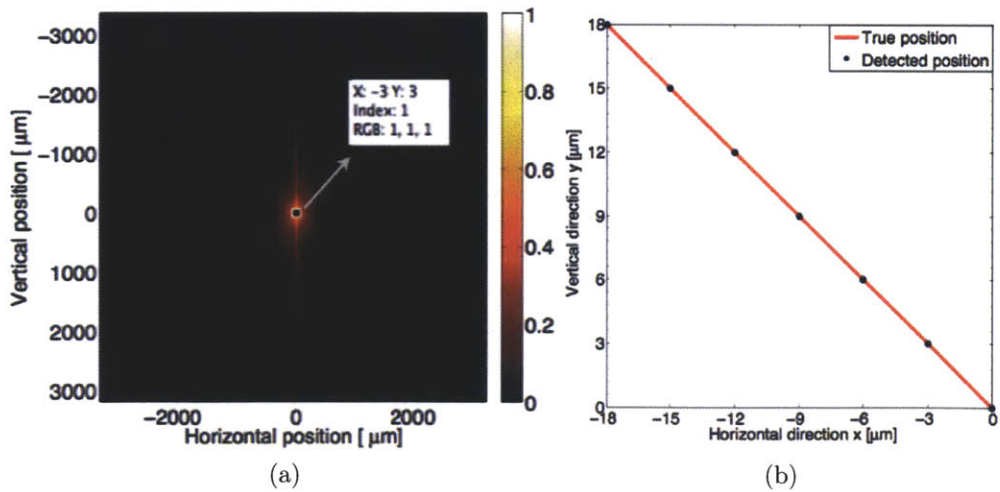


Figure 4-6: (a) Normalized cross-correlation result between two consecutive reconstructions; (b) Detected positions of the shim object at each step.

Chapter 5

Conclusions and Future work

With the fast development in semiconductor fabrication field, CCD and CMOS cameras with high sampling rate, high frame rate and large dynamic range become available. Furthermore, advances in computing apparatus made the implementation of complex algorithm clear and efficient. By combining these technologies with classical optics, computational imaging becomes the trend of optics for the next generation.

One of the most important computational imaging techniques, digital holography, has been studied in this thesis. Digital holography has been widely used to reconstruct 3D profiles of objects from a single intensity frame. During the free space propagation of the object field in holography, the information of the object is spread out onto the entire digital sensor. Compared to the traditional point-to-point imaging technique, taking advantage of information spreading in holography can greatly increase the chance to detect small motions of objects. In this thesis, we studied how to use digital holography to detection object's sub-pixel movement.

In the case of detecting sub-pixel movement or locating object with sub-pixel

accuracy, the information is under-sampled. To tackle this problem, compressive sensing theorem has been implemented here together with digital holography. Compressive sensing says that if a signal is sparse, it can be accurately reconstructed even from a small amount of linear measurements. Surely, the number of measurements has a lower bound, which is inversely proportional to the sparsity of the signal as well as the “incoherence” parameter that measures how incoherent the sensing matrix and the sparsifying basis are relative to each other. The solution of compressive sensing is also robust to noise.

Considering that most of the general objects are not sparse, here we chose different sparsifying bases to convert general signals to sparse signals. For a 1D object signal, the derivative operator is a good choice. However, since the 2D equivalent would constitute a Hilbert transform that does not exist, so a different sparsifying basis, namely the spiral phase mask, was implemented to sparsify a general 2D object. By implementing the sparsifying bases, compressive reconstruction can successfully reconstruct the edges of the object directly from the hologram captured in the experiment, free from artifacts due to twin image and other sources of noise. The experimental results also show that $1/45$ sub-pixel movement can be successfully detected in the 1D case through compressive holography and 12nm accuracy can be achieved. In the 2D case, our success so far was equipment-limited to a sub-pixel gain of only 4; this is due to memory limitation in zero-padding of the 2D Fourier transform. This can be easily overcome in the future versions.

An additional natural direction for the future work, how to implement compressive holography in super-localization along the optical axis will be an interesting topic.

Bibliography

- [1] J. A. Dominguez-Caballero, “Digital holographic imaging of aquatic species,” Master’s thesis, Massachusetts Institute of Technology (2006).
- [2] B. Javidi and E. Tajahuerce, “Three-dimensional object recognition by use of digital holography,” *Opt. Lett.* **25**, 610–612 (2000).
- [3] S. H. Lee, Y. Roichman, G. R. Yi, S. H. Kim, S. M. Yang, A. van Blaaderen, P. van Oostrum, and D. G. Grier, “Characterizing and tracking single colloidal particles with video holographic microscopy,” *Opt. Express* **15**, 18275–18282 (2007).
- [4] U. Schnars and W. Jueptner, *Digital Holography: Digital Hologram Recording, Numerical Reconstruction, and Related Techniques* (Springer, 2005).
- [5] L. Tian, N. Loomis, J. A. Domínguez-Caballero, and G. Barbastathis, “Quantitative measurement of size and three-dimensional position of fast-moving bubbles in air–water mixture flows using digital holography,” *Appl. Opt.* **49**, 1549–1554 (2010).
- [6] L. Tian, N. Loomis, J. A. Dominguez-Caballero, and G. Barbastathis, “Bubble size measurement in high-density air-water mixture flows with wide size distributions using digital holography,” in “Frontiers in Optics,” (Optical Society of America, 2009), p. FThB1.
- [7] T. Zhang and I. Yamaguchi, “Three-dimensional microscopy with phase-shifting digital holography,” *Opt. Lett.* **23**, 1221–1223 (1998).
- [8] L. Tian, H. Gao, and G. Barbastathis, “Digital holographic imaging of multi-phase flows,” in “Computational Optical Sensing and Imaging,” (Optical Society of America, 2011), p. CWB5.
- [9] Y. Pu and H. Meng, “Four-dimensional dynamic flow measurement by holographic particle image velocimetry,” *Appl. Opt.* **44**, 7697–7708 (2005).
- [10] M. T. Özgen, “Analysis of in-line Fresnel holograms via chirp separation,” *Optical Engineering* **45**, 035801–+ (2006).

- [11] W. Li, N. Loomis, Q. Hu, and C. S. Davis, "Focus detection from digital in-line holograms based on spectral $l(1)$ norms," *J. Opt. Soc. Am. A* **24**, 3054–3062 (2007).
- [12] D. J. Brady, K. Choi, D. L. Marks, R. Horisaki, and S. Lim, "Compressive holography," *Opt. Express* **17**, 13040–13049 (2009).
- [13] M. T. Wei and A. Chiou, "Three-dimensional tracking of brownian motion of a particle trapped in optical tweezers with a pair of orthogonal tracking beams and the determination of the associated optical force constants," *Opt. Express* **13**, 5798–5806 (2005).
- [14] A. Yildiz, J. N. Forkey, S. A. McKinney, T. Ha, Y. E. Goldman, and P. R. Selvin, "Myosin V walks hand-over-hand: single fluorophore imaging with 1.5-nm localization," *Science* **300**, 2061–2065 (2003).
- [15] M. J. Saxton and K. Jacobson, "Single-particle tracking: applications to membrane dynamics," *Annu. Rev. Biophys. Biomol. Struct.* **26**, 373–399 (1997).
- [16] M. K. Cheezum, W. F. Walker, and W. H. Guilford, "Quantitative comparison of algorithms for tracking single fluorescent particles," *Biophysical Journal* **81**, 2378 – 2388 (2001).
- [17] G. Dehnhardt, B. Mauck, W. Hanke, and H. Bleckmann, "Hydrodynamic trail-following in harbor seals (*phoca vitulina*)," *Science* **293**, 102–104 (2001).
- [18] H. Beem, J. Dahl, and M. Triantafyllou, "Harbor seal vibrissa morphology reduces vortex-induced vibrations," *Proceedings of the 64th Annual Meeting of the DFD* **56** (2011).
- [19] G. Vendroux and W. G. Knauss, "Submicron deformation field measurements: Part 2. improved digital image correlation," *Exp. Mech.* **38**, 86–92 (1998).
- [20] T. C. Chu, W. F. Ranson, and M. A. Sutton, "Applications of digital-image-correlation techniques to experimental mechanics," *Experimental Mechanics* **25**, 232–244 (1985).
- [21] P. Zhou and K. E. Goodson, "Subpixel displacement and deformation gradient measurement using digital image/speckle correlation (disc)," *Opt. Eng.* **40**, 1613–1620 (2001).
- [22] P. Thevenaz, U. Ruttimann, and M. Unser, "A pyramid approach to subpixel registration based on intensity," *Image Processing, IEEE Transactions on* **7**, 27–41 (1998).
- [23] S. J. Timoner and D. M. Freeman, "Multi-image gradient-based algorithms for motion estimation," *Optical Engineering* **40**, 2003–2016 (2001).

- [24] H. Takeda, P. Milanfar, M. Protter, and M. Elad, “Super-resolution without explicit subpixel motion estimation,” *IEEE Trans. Image Process.* **18** (2009).
- [25] H. Ur and D. Gross, “Improved resolution from subpixel shifted pictures,” *Comput. Vis. Graph. Image Process.* **54**, 181–186 (1992).
- [26] A. Ashok and M. A. Neifeld, “Pseudorandom phase masks for superresolution imaging from subpixel shifting,” *Appl. Opt.* **46**, 2256–2268 (2007).
- [27] E. Candès and J. Romberg, “Sparsity and incoherence in compressive sampling,” *Inverse Probl.* **23**, 969 (2007).
- [28] E. Candès and Y. Plan, “A Probabilistic and RIPless Theory of Compressed Sensing,” *IEEE Trans. Inf. Theory* **57**, 7235–7254 (2011).
- [29] D. L. Donoho, “Compressed sensing,” *IEEE Trans. Inform. Theory* **52**, 1289–1306 (2006).
- [30] E. Candès, J. Romberg, and T. Tao, “Robust uncertainty principles: exact signal reconstruction from highly incomplete frequency information,” *IEEE Trans. Inf. Theory* **52**, 489–509 (2006).
- [31] E. Candès, J. Romberg, and T. Tao, “Stable Signal Recovery from Incomplete and Inaccurate Measurements,” *Comm. Pure Appl. Math.* **59**, 1207–1223 (2006).
- [32] L. Tian, J. Lee, S. B. Oh, and G. Barbastathis, “Experimental compressive phase space tomography,” *Opt. Express* **20**, 8296–8308 (2012).
- [33] J. M. Bioucas-Dias and M. A. T. Figueiredo, “A new TwIST: two-step iterative shrinkage/thresholding algorithms for image restoration,” *IEEE Trans. Image Process.* **16**, 2992–3004 (2007).
- [34] L. Kuptsov, “Einstein rule,” *Encyclopedia of Mathematics* (2001).
- [35] A. Jesacher, S. Fürhapter, S. Bernet, and M. Ritsch-Marte, “Shadow effects in spiral phase contrast microscopy,” *Physical Review Letters* **94** (2005).
- [36] G. Situ, G. Pedrini, and W. Osten, “Spiral phase filtering and orientation-selective edge detection/enhancement,” *J. Opt. Soc. Am. A* **26**, 1788–1797 (2009).
- [37] T. J. McIntyre, C. Maurer, S. Bernet, and M. Ritsch-Marte, “Differential interference contrast imaging using a spatial light modulator,” *Opt. Lett.* **34**, 2988–2990 (2009).
- [38] S. Fürhapter, A. Jesacher, C. Maurer, S. Bernet, and M. Ritsch-Marte, “Spiral phase microscopy,” *ADV IMAG ELECT PHYS* **146** (2007).
- [39] K. G. Larkin, D. J. Bone, and M. A. Oldfield, “Natural demodulation of two-dimensional fringe patterns. i. general background of the spiral phase quadrature transform,” *J. Opt. Soc. Am. A* **18**, 1862–1870 (2001).